Nanoscale Advances

ROYAL SOCIETY OF CHEMISTRY

PAPER

View Article Online
View Journal | View Issue

Cite this: *Nanoscale Adv.*, 2025, **7**, 4056

Biomass-derived carbon supported cobalt-phospho-boride as a bifunctional electrocatalyst for enhanced alkaline water splitting†

B. Sirichandana,[ab] R. Silviya,[c] S. Venkataprasad Bhat,[d] Nainesh Patel[c] and Gurumurthy Hegde *[ab]

Received 3rd March 2025
Accepted 9th May 2025

DOI: 10.1039/d5na00213c

rsc.li/nanoscale-advances

Developing efficient and low-cost bifunctional electrocatalysts for overall water splitting in order to reduce the future energy crisis is crucial and challenging. Herein, a facile two-step fabrication *via* pyrolysis and chemical reduction was used for the synthesis of biomass-derived carbon-based electrocatalyst (MT) from mulberry bark and its subsequent modification with cobalt phospho-boride (MT/CoPB) for efficient bifunctional electrocatalysis in alkaline media. The effect of *B*/*P* ratios and carbon-to-metal ratios on electrocatalytic performance of HER was investigated. Notably, the optimized MT/CoPB catalyst (*B*/*P* = 5, C : M = 2 : 1) exhibited a lower overpotential of −86 mV for HER and 310 mV for OER to reach the current density of 10 mA cm^{-2}. The robust electrocatalytic performance of MT/CoPB towards the HER and OER was attributed to the combined effect of carbon and CoPB. Notably, it achieved a low cell voltage of 1.59 V to reach a current density of 10 mA cm^{-2}, also maintaining reliable long-term stability. Characterization studies revealed that the enhanced performance was due to the amorphous structure of the catalyst, high electrochemical surface area, and efficient charge transfer. This work demonstrates the potential of biomass-derived carbon-based materials in the development of cost-effective and durable electrocatalysts for water splitting and green hydrogen production.

1. Introduction

In recent years, fossil fuels have served as the dominant energy source. However, with technological advancement, the demand for fossil fuels has surged significantly. As a consequence, the depletion of these energy resources and environmental pollution have become critical concerns.[1] Hydrogen is gaining significant global momentum as an energy carrier and clean fuel, playing a key role in reaching "net-zero" emission targets. Among the various methods, production of green hydrogen stands out as the most promising pathway for achieving deep decarbonization and supporting worldwide efforts to meet "net-zero" goals.[2] In this context, electrochemical water splitting presents a key solution for sustainable energy by offering a clean method to produce hydrogen using renewable energy. The process involves two primary reactions: the hydrogen evolution reaction (HER) at the cathode and the oxygen evolution reaction (OER) at the anode in an electrolyzer.[3] The hydrogen generated can be used in fuel cells, providing an eco-friendly alternative to fossil fuels, with water as the sole byproduct, thereby, making it a sustainable source of energy.[4] The sluggish kinetics of water splitting lead to high overpotentials and reduced efficiency, prompting efforts to design high-performance electrocatalysts to lower energy consumption. Pt, Ir and Ru are the precious metal-based electrocatalysts, which are proven to be the state of the art of catalysts.[5] However, the key challenges include the limited availability and the high cost of precious metal based electrocatalysts, limiting their widespread use and development.[6] Consequently, developing efficient, affordable, and environmentally friendly electrocatalysts is crucial.

In the past decade, transition-metal oxides,[7] sulphides,[8] phosphides,[9,10] nitrides,[11] carbides,[12] selenides,[13] borides[14] based compounds have shown great potential in water-splitting reactions. Apart from these transition metal-based materials, metal–organic frameworks have also been studied by researchers for water splitting.[15] Metal borides have emerged as a cutting-edge class of materials, attracting significant interest in nanotechnology and materials science due to their exceptional mechanical, thermal, and electronic properties. The unique combination of metal and boron at the nanoscale imparts these materials with good electrical conductivity,

[a]*Department of Chemistry, Christ University, Hosur Road, Bengaluru, 560029, India*
[b]*Centre for Advanced Research and Development (CARD), Christ University, Hosur Road, Bengaluru, 560029, India. E-mail: murthyhegde@gmail.com*
[c]*Department of Physics and Electronics, Christ University, Hosur Road, Bengaluru, 560029, India*
[d]*Green Energy Materials (GEM) Laboratory, Department of Physics and Nanotechnology, SRM Institute of Science and Technology (Deemed to be University), Kattankulathur, Tamil Nadu, India*

† Electronic supplementary information (ESI) available. See DOI: https://doi.org/10.1039/d5na00213c

remarkable hardness, excellent thermal stability, and enhanced toughness, making them ideal for a wide range of advanced technological applications. Over the years, metal borides have been investigated for their electrochemical applications. Furthermore, the development of both B-rich and B-deficient transition metal borides (TMBs), incorporating precious and non-precious metals, has led to significant progress in catalytic applications for other vital processes such as carbon dioxide reduction (CO_2RR), nitrogen reduction (NRR), and oxygen reduction (ORR).[16] In particular, TMBs have gained considerable attention in electrocatalysis due to their unique structural and electronic versatility. Their amorphous forms provide a high density of catalytically active sites, which can be tuned to enhance bifunctional activity in critical electrochemical reactions such as the hydrogen evolution reaction (HER) and oxygen evolution reaction (OER). With their tunable properties, cost-effectiveness, and multifunctionality, TMBs continue to demonstrate immense potential as next-generation electrocatalysts for sustainable energy conversion and storage systems.

Transition metals have properties of high activity towards water splitting while restricted by poor stability and low conductivity. In order to overcome these issues carbon-based materials are extensively studied. Carbon forms such as carbon nanotubes,[17] graphene[18] or reduced graphene oxide[19] are explored due to their excellent stability and conductivity. Integrating carbon nanomaterials and transition metals can effectively overcome the concerns encountered in transition metal-based electrocatalysts.[20,21] Carbon-based electrocatalysts with transition metals (Ni, Co, Mo, and others) in the form of metal oxides, dichalcogenides, metal carbides, and metal phosphides have been reported for HER and/or OER.[22–24] Carbon nanomaterials are conventionally produced using fossil fuel-derived precursors, which typically involve energy-intensive synthesis processes.[25] Due to ever-growing technological advancement, tons of wastes are left behind in the environment. Among various waste materials, biomass-based waste materials have gained attention as a sustainable, carbon-rich resource for the fabrication of carbon materials due to their uniform size, good electronic conductivity, tunable porosity, controlled morphology, remarkable stability and cost effectiveness. These desirable properties make them highly suitable for a wide range of electrochemical applications. Notably, the physicochemical characteristics of these materials are dependent on both the specific biomass precursor and the synthesis technique utilized. Typically, these materials exhibit a high density of structural defects (edges) within a disordered carbon matrix, which numerous studies have identified as key contributors to their strong electrocatalytic activity.[26]

For instance, nickel diselenide nanoparticles embedded in carbon derived from green apple peels have been synthesized as electrocatalysts for HER.[27] Cobalt oxide nanoparticles embedded in nitrogen doped carbon, synthesized from spent coffee grounds as the precursor, has been reported as an electrocatalyst for the HER.[28] Another study highlights cobalt phosphide (CoP) loaded onto a nitrogen, sulfur, and phosphorus co-doped carbon matrix (CoP@NSPC), produced *via* carbothermic reduction using ginkgo leaf, as an electrocatalyst for HER.[29] Additionally, cobalt and tungsten loaded nitrogen-doped porous carbon based electrocatalysts, obtained from silk fibroin have been reported.[30] Apart from the above-mentioned forms of carbon, carbon nanospheres (CNS) are formed by the combination of pentagonal and heptagonal carbon rings.[31] In their spherical form, the graphite sheets appear as waving flakes that follow a spherical structure, resulting in exposed edges on the surface which are expected to be chemically active.[32] This structure makes CNS a promising material for various electrochemical applications.[33,34] However, the utilization of biomass as a precursor for the synthesis of CNS is less explored, despite its advantages of being widely available, a sustainable source, and the cost-effectiveness of biomass source, whose main components include cellulose, hemicellulose, and lignin.[35] Apart from the high surface area, uniform shape, size, and high stability, the porous structure of carbon derived from biomass[36] enhances interfacial electron transfer, which aids in water splitting.

It has been reported that cobalt boride performed effective electrocatalytic activity for HER and OER in comparison with other non-noble transition metal borides[37] and the synergic effect of Co–P and Co–B in CoPB has enhanced HER and OER.[38] In this work biomass-derived CNS and cobalt phospho boride are integrated by simple two-step synthesis for efficient HER and OER. Mulberry is cultivated across diverse climatic conditions, with its primary cultivation area located in the tropical zone, particularly in Karnataka, India. It is a highly versatile tree which is mainly used for silkworm rearing. Additionally, mulberry twigs and wood stems are utilized in cosmetic products, including hair lotions and skin moisturizers, as well as in wood processing for furniture. Herein, Mulberry bark, with 23.64% lignin and 67.26% holocellulose[39] was chosen as a biomass precursor to synthesize CNS. Mulberry bark-derived carbon nanosphere (MT) was synthesized by pyrolysis without adding any dopants or activating agents. Further, MT-supported cobalt phospho-boride was synthesized using a simple chemical reduction method to obtain the electrocatalyst MT/CoPB. The optimized catalyst was subjected to electrochemical studies to evaluate its performance for HER and OER. The optimized catalysts are compared with CoB, CoPB, and MT/CoB to examine the effect of the synthesized carbon nanospheres on electrocatalytic activity. To examine the real-time application, durability, and stability studies were also examined. This research opens up new possibilities for the design of efficient, sustainable, and cost effective electrocatalysts for green hydrogen production.

2. Experimental

2.1. Chemicals and reagents

Potassium hydroxide pellets (KOH, 99%), cobalt chloride hexahydrate ($CoCl_2 \cdot 6H_2O$, 99%), sodium borohydride ($NaBH_4$, 98%), sodium hypophosphite ($NaH_2PO_2 \cdot H_2O$, 99%), were purchased from Research Lab. Conc HCl used is from Thomas Baker, ethanol was obtained from Finar Chemicals and deionized (DI) water was used as the general-purpose solvent.

2.2. Synthesis of carbon nanospheres

Mulberry bark (MT-Raw) was the biomass precursor used for the synthesis of CNS. The precursor was washed with water, dried in sunlight to eliminate moisture content, ground to fine powder, and sieved in a 75 μm sieve to obtain uniform particle size. The sieved precursor taken in the crucible was subjected to pyrolysis in a quartz tube furnace at 1000 °C with continuous nitrogen flow. The obtained carbonized material was washed using 0.1 N HCl, followed by water and ethanol wash and dried in a hot air oven. The CNS obtained at 1000 °C labelled as (MT) was taken for further studies.

2.3. Synthesis of MT/CoPB

In a beaker containing 20 mL of DI water, the synthesized MT and $CoCl_2 \cdot 6H_2O$ were added in varying carbon to metal (C : M) weight ratios of 1 : 1, 2 : 1, and 3 : 1. To this solution, NaH_2PO_2 as a mild reducing agent and source of phosphorus, and $NaBH_4$ as a strong reducing agent and boron source were added and stirred for 10 min. The addition of $NaBH_4$ led to effervescence followed by the formation of black precipitate. The stirring was continued until the bubbles ceased. The obtained precipitate was thoroughly washed with distilled water and ethanol. To ensure complete reduction, the combined molar ratio of NaH_2PO_2 and $NaBH_4$ to Co was maintained five times. The *B*/*P* ratio was optimized by modifying the molar concentration of $NaBH_4$ and NaH_2PO_2. For comparison studies, CoB and CoPB were synthesized without MT, while MT/CoB was synthesized in the absence of NaH_2PO_2 in a similar process. The detailed procedure is presented in ESI.†

2.4. Materials characterization

Micro-Raman spectroscopy was performed using a Renishaw system (Horiba Model: Lab RAM HR) with a 532 nm laser excitation wavelength. Energy dispersive X-ray spectroscopy (EDS) analysis and Field emission scanning electron microscopy (FESEM) were performed using an Apero system (Thermo Fisher Scientific, USA) in order to verify the presence and relative abundance of elements and to assess the morphology of the catalysts. X-ray diffraction (XRD) analysis was carried out using a Rigaku Miniflex 600 (Rigaku, Japan) with Cu-Kα radiation. Fourier-transform infrared (FT-IR) spectra were acquired using an IRSpirit-L (SHIMADZU, Japan). Transmission Electron Microscopy (TEM) analysis of the compounds was carried out using JEOL Japan, JEM-2100 Plus. X-ray Photoelectron spectroscopy (XPS) measurements were performed using a PHI Versaprobe III scanning XPS microprobe, Physical Electronics, USA.

2.5. Electrochemical measurements

A homogeneous catalyst ink was prepared by addition of 5 mg of the catalyst in 1 mL of ethanol and then subjected it to sonication. Binder was prepared by the addition of 40 μL of Nafion (5 wt%) in 1 mL ethanol. Initially, 10 μL of the as prepared binder is deposited on a 3 mm polished glassy carbon electrode, followed by deposition of 20 μL of catalyst ink by drop casting method. All the electrochemical measurements were performed in potentiostat from CH instruments (CH16011E). The studies were done in three electrode systems with saturated calomel electrode (SCE) as the reference electrode, catalyst-deposited glassy carbon electrode (GCE) as the working electrode and graphite rod as the counter electrode. 1 M KOH was used as the electrolyte for all measurements. The linear sweep voltammetry (LSV) studies for HER were carried out in the potential range of −1.4 V to −1.06 V (*vs.* SCE) and for OER in the potential range of 0 V to 0.8 V (*vs.* SCE) at the scan rate of 10 mV s^{-1}. Prior to HER tests, a chronoamperometry test was performed till the steady current was obtained to ensure the removal of surface oxides formed on the catalyst. The measured potentials were converted to reversible hydrogen electrode (RHE) with the aid of the Nernst equation, $E = E_o + (0.059 \times \text{pH})$ where $E_o = 0.241$ V for saturated calomel electrode. Cyclic voltammetry (CV) was performed in order to obtain electrochemical surface area (ECSA) from double layer capacitance (C_{dl}) at different scan rates of 20, 40, 60, 80, 100, and 120 mV s^{-1} in non-faradaic regions. To obtain the C_{dl} values, the slope was derived by performing a linear fit on the plot of the scan rates against the difference between cathodic and anodic current densities. The solution resistance (R_s) and charge transfer resistance (R_{ct}) were determined by fitting the semicircle of the Nyquist plot, which was acquired through electrochemical impedance spectroscopy (EIS) in a frequency range of 100 kHz to 1 Hz. All the polarization curves were *iR*-corrected. The overall water splitting was investigated in a two-electrode system by using MT/CoPB deposited on GCE as both electrodes.

Results and discussion

Biomass-derived carbon (MT) was synthesized using mulberry bark as a precursor by pyrolysis at 1000 °C[40] under a nitrogen atmosphere without using any activating agents. Further carbon supported cobalt phospho-boride (MT/CoPB) was synthesized by a simple chemical reduction method. For the optimization of the catalyst the *B*/*P* molar ratio and C : M weight ratio were varied in MT/CoPB. Optimized electrocatalyst, with *B*/*P* of 5 and C : M of 2 : 1, illustrated the best electrocatalytic activity for HER, as discussed later. The optimal MT/CoPB were henceforth subjected to characterization techniques and tested for electrochemical water splitting. The presence of functional groups, such as C–O and O–H, of lignocellulosic components in mulberry bark precursor (MT-Raw) along with C–C bond was confirmed from FTIR spectra (Fig. S1†). The FTIR analysis of MT (Fig. S1†) revealed that the functional group peaks disappear after pyrolysis at 1000 °C except for C–C bonds, indicating an increase in carbon content due to the removal of volatile components from the precursor.

The XRD pattern of the synthesized MT (Fig. 1a) shows two dominant broad peaks at approximately $2\theta = 24°$ and 44° which corresponds to (002) and (100) planes of carbon respectively.[41] These peaks are assigned to the parallel stacking of graphene sheets and to sp^2 hybridized carbons.[42] The XRD pattern of MT/CoPB (Fig. 1a) shows a lack of crystalline peaks, which confirms the amorphous nature of the catalyst. The disappearance of the

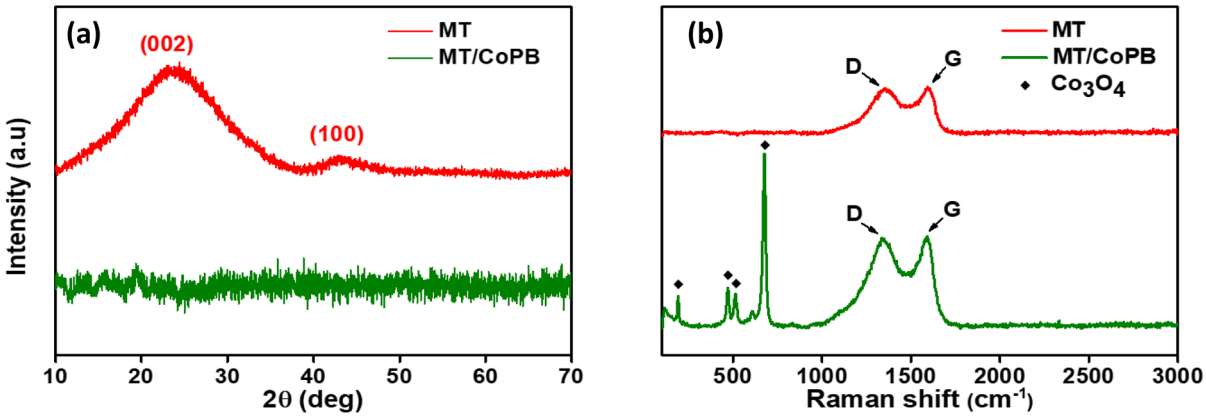

Fig. 1 (a) XRD pattern and (b) Raman spectrum of MT and MT/CoPB.

broad carbon peaks post-synthesis is not due to the removal or degradation of the carbon substrate, but rather due to peak broadening caused by the amorphous and surface-rich nature of the CoPB product. The amorphous nature of MT/CoPB is also validated by the SAED pattern (Fig. 2f). Amorphous materials possess a greater number of undercoordinated atoms, which often act as catalytically active sites. This leads to an increased electrochemical surface area and a larger electrolyte–electrocatalyst interface compared to crystalline materials of the same mass.[43]

The Raman spectrum of the MT and MT/CoPB is presented in Fig. 1b. The Raman spectra of MT show bands nearly at 1352 cm^{-1} and 1593 cm^{-1}, representing the D and G bands of graphitic carbon, respectively, with an I_D/I_G ratio of 0.98. The D-band signifies structural disorder in the carbon lattice, while the G-band is associated with the E_{2g} vibrational mode of sp^2-hybridized carbon atoms.[44] The Raman spectrum of MT/CoPB maintains the bands assigned to D (1348 cm^{-1}) and G (1590 cm^{-1}) bands of carbon with an I_D/I_G ratio of 0.99. Bands at approximately 186, 464, 510, 594 and 670 cm^{-1} correspond to the different modes of Co_3O_4.[45] This surface oxide formation on MT/CoPB is due to *ex situ* synthesis and exposure of the catalyst to the atmosphere before measurement. However, during HER, the surface oxides are reduced in the initial cycles, and the metallic catalytic sites are exposed, and during OER, they are converted to active oxy-hydroxy species (discussed later). Therefore, these surface oxide layers do not create any obstacle to the catalytic activity. The morphology of the synthesized MT and MT/CoPB were examined using FESEM, as shown in Fig. 2a and d, respectively. The morphology of MT displays the graphitic carbon layer with embedded spherical nanoparticles (Fig. 2a and S2†). The EDS analysis shows 85.5% of carbon as

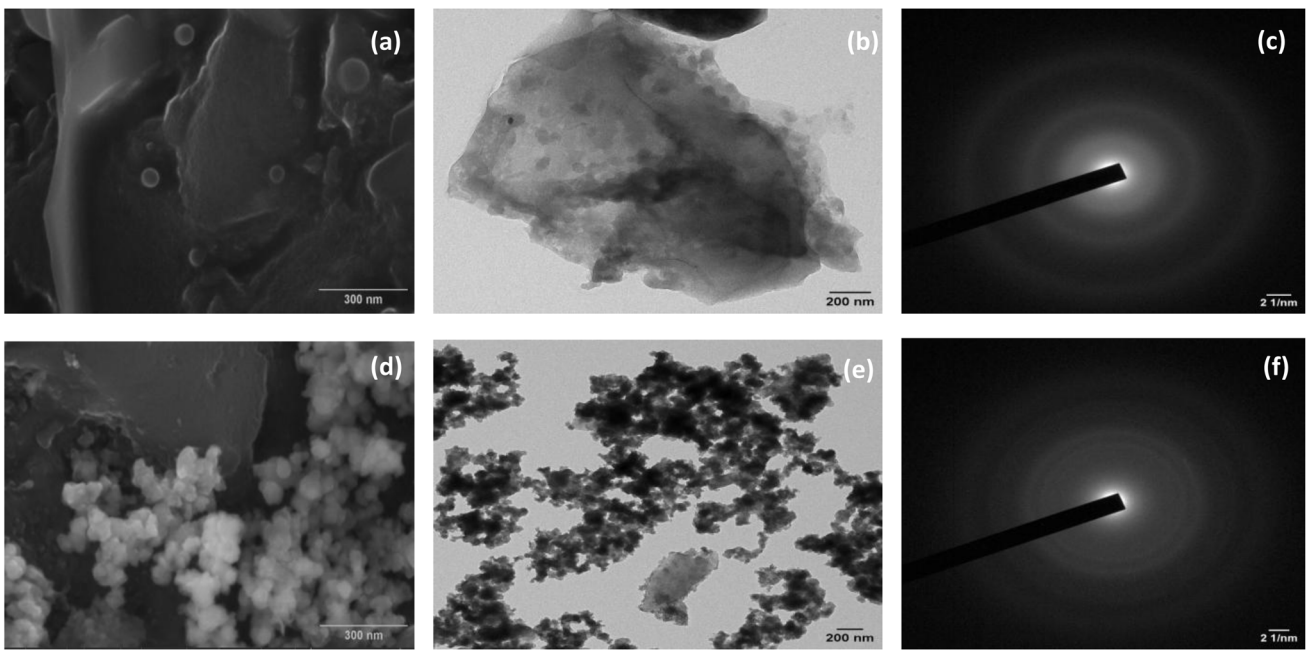

Fig. 2 FESEM images (a) and (d), TEM images (b) and (e), SAED patterns (c) and (f) of MT and MT/CoPB, respectively.

a major component and 15.5% of O (Fig S3a).† The FESEM analysis of MT/CoPB shows the deposition of spherical particles of CoPB on the carbon surface (Fig. 2d and S2†) and the elemental composition from EDS is given in (Fig. S3b†). The CoPB particles are well-dispersed on the carbon matrix owing to the dangling bonds on the surface which anchors them.[31] The elemental mapping (Fig. S4†) clearly distinguishes the CoPB particles from the carbon with a relatively uniform distribution of the elements in CoPB nanoparticles in the catalyst MT/CoPB. The embedded nanospheres of MT were further corroborated by the TEM image (Fig. 2b) with a particle size in the range of 55–60 nm. The TEM image (Fig. 2e) of MT/CoPB illustrates the distribution of spherical particles of CoPB on the carbon matrix, and the morphology of MT remains intact even after the incorporation of CoPB. The SAED pattern of MT (Fig. 2c) and MT/CoPB (Fig. 2f) demonstrates the amorphous nature as illustrated by the presence of diffused rings.

The chemical states and elemental composition of the MT and the electrocatalyst MT/CoPB were investigated by XPS measurements. The XPS survey spectrum of MT (Fig. S5a†) indicates the presence of C 1s and O 1s peaks. A deconvoluted C 1s spectrum of MT consists of four individual component peaks (Fig. 3a) corresponding to sp^3 C–C (283.8 eV), sp^2 C=C (284.5 eV), C–O (285.8) and C=O (288.5).[46–48] Similarly, the O 1s spectrum (Fig. 3b) is deconvoluted into three distinct components corresponding to C=O (530.6), C–O (532.29) and O=C–O (533.5).[48] The representative survey spectrum of MT/CoPB (Fig. S5b†) reveals the presence of C, O, Co, B, and P. The XPS data for the MT/CoPB showed the following atomic percentages: 5.85% B, 41.04% C, 36.71% O, 1.52% P, and 14.88% Co, resulting in a C : M ratio of ~2 : 1 and a *B*/*P* ratio close to ~5 : 1. The oxygen content is predominant because of the exposure of the electrocatalysts to air but this does not indicate instability of the material in air. Rather, it reflects a surface-level transformation that is commonly observed in metal phosphides and boride systems upon ambient exposure. It is well established that transition metal borides and phospho-borides form a native oxide/hydroxide shell upon exposure to air, resulting in a core@shell structure where the shell comprises Co–O or Co–OH species, and the core retains the original boride phase.[49] The peak positions of C 1s spectra of MT/CoPB (Fig. 3c) were found to be similar to MT, which indicates the presence of carbon in the catalyst. Co 2p level was deconvoluted to multiple peaks (Fig. 3d) with a binding energy (BE) at 777.5 eV corresponding to elemental cobalt (Co^0) and at 780.9 eV and 782.7 eV attributed to trivalent (Co^{3+}) and divalent (Co^{2+}) respectively. A negative shift of 0.6 eV is detected in the BE for the Co^0 peak in MT/CoPB as compared to pure metallic cobalt (778.1 eV), implying higher electron density on the cobalt sites. The presence of oxidized cobalt is attributed to the *ex situ* catalyst. The satellite peaks are also observed for Co $2p_{3/2}$, corresponding to oxidized cobalt. Two peaks at 187.4 eV and 191.4 eV in the B 1s spectrum (Fig. 3e), indicates elemental boron and oxidized boron, respectively. The BE values show a positive shift of 0.3 eV in comparison to pure boron (187.1 eV), suggesting a partial electron loss from boron. Similarly, the P 2p spectrum shows peaks at 129.6 eV and 132.5 eV, attributed to elemental phosphorus and oxidized phosphorus, respectively, as shown in Fig. 3f. The lower BE of elemental phosphorus compared to the reported value (130.2 eV) indicates partial electron transfer toward phosphorus.[38] This unique behaviour of CoPB where transfer of electrons takes place from Co to P whereas B loses electrons to Co, thereby making it rich in electrons. This combined effect helps to maintain optimal electron density on cobalt sites, which helps in improving the electrocatalytic activity. As there is no bond formation observed in XPS between

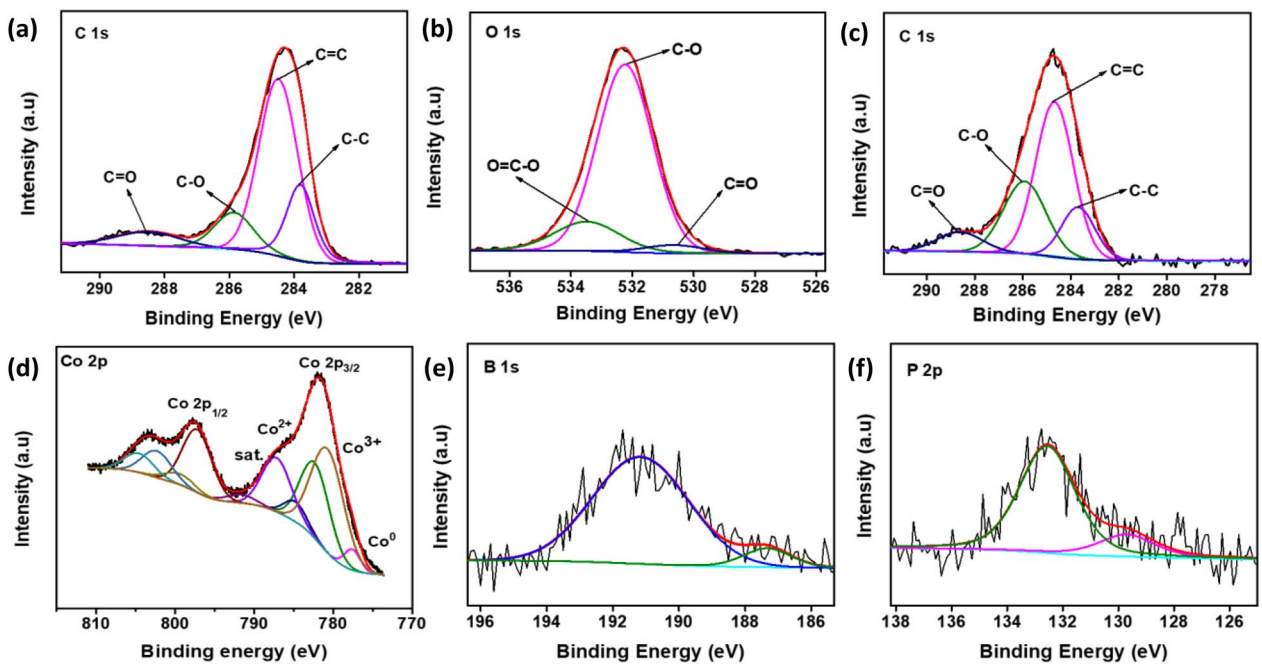

Fig. 3 XPS spectra of (a) C 1s, (b) O 1s for MT and (c) C 1s, (d) Co 2p, (e) B 1s, (f) P 2p for MT/CoPB.

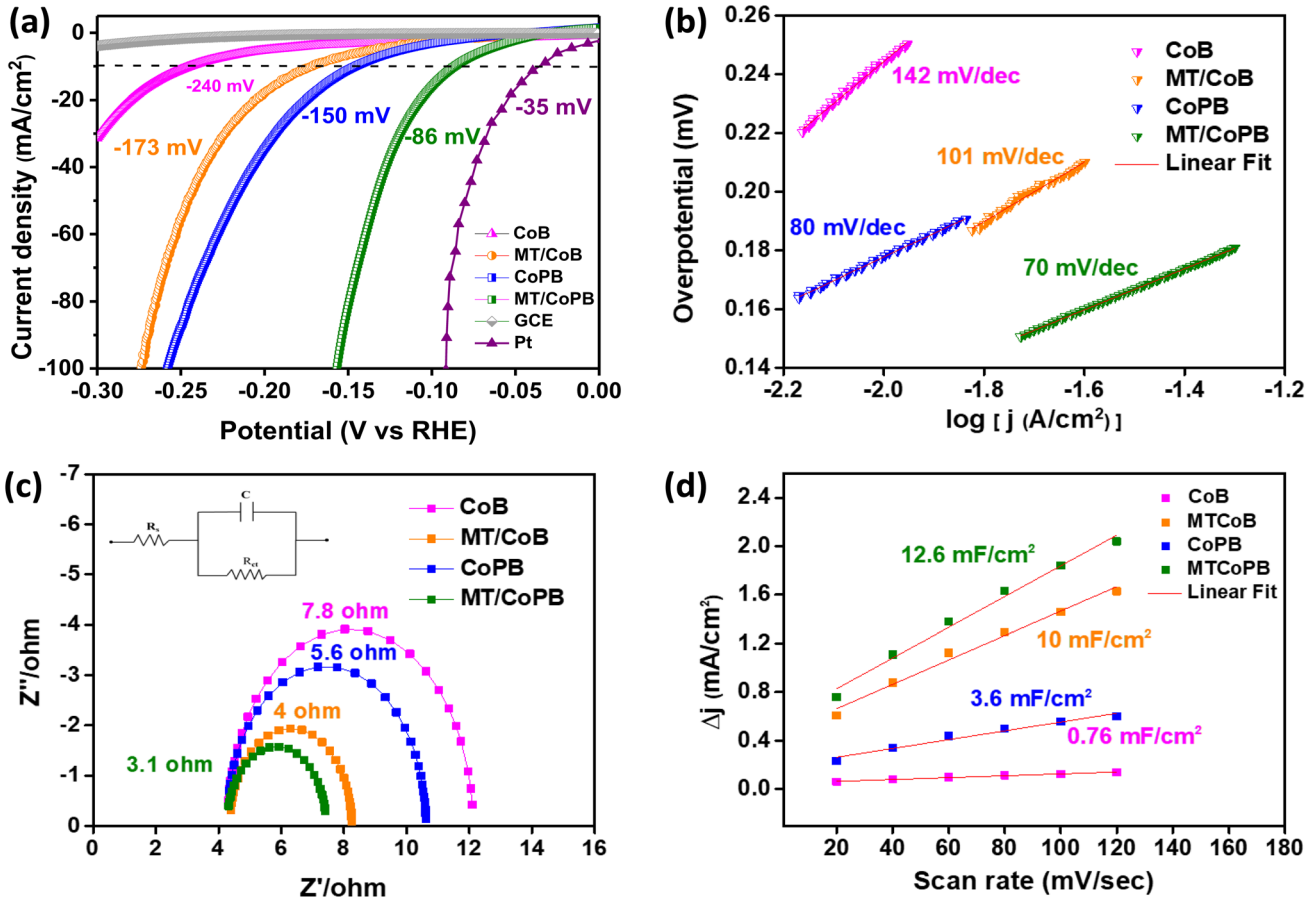

Fig. 4 (a) Linear polarization curves (b) Tafel plot (c) Nyquist plot (d) a plot illustrating the differences in cathodic and anodic current densities at different scan rates to assess the C_{dl} values for HER.

CoPB and MT it can be concluded that the electronic interaction similar to metal-support interaction exists between MT and CoPB.[50,51]

The electrochemical performance of the synthesized catalysts was tested for HER in an alkaline medium of 1 M KOH. Linear sweep voltammetry measurement was employed to obtain the polarization curves at a scan rate of 10 mV s^{-1} in the potential range of 0 V to −0.3 V (*vs.* RHE). The composition of the catalyst was optimized by varying the *B*/*P* molar ratio and C : M weight ratios in MT/CoPB. Previous studies demonstrated that a *B*/*P* ratio of 5 in CoPB resulted in optimal electrocatalytic activity. Therefore, the C : M weight ratios were varied to 1 : 1, 2 : 1, and 3 : 1 while maintaining the *B*/*P* ratio at a constant value of 5. The overpotentials measured were −130 mV, −86 mV, and −223 mV at 10 mA cm^{-2} current density for C : M of 1 : 1, 2 : 1, and 3 : 1, respectively (Fig. S6a†). With a C : M ratio of 2 : 1, the overpotential is lowest, suggesting an optimal balance between electrical conductivity from carbon and active sites from CoPB, enhancing catalytic efficiency. The Nyquist plot for C : M variation is depicted in Fig. S6b,† which suggests that the optimal performance observed at a 2 : 1 C : M ratio of MT/CoPB is due to the low R_{ct} value. In the next step, the *B*/*P* ratio in MT/CoPB was varied by maintaining the amount of Co and carbon constant. The electrocatalyst with *B*/*P* = 1, 3, 5, and 7, as illustrated in Fig. S6c,† showed an overpotential of −147 mV, −132 mV, −86 mV and −156 mV, respectively, at 10 mA cm^{-2} current density for HER. The corresponding charge transfer resistance was recorded to be 6.1 Ω, 5.2 Ω, 3.1 Ω, and 6.7 Ω (Fig. S6d†), respectively. It can be noticed that with the increase in the *B*/*P* ratio, catalytic activities of MT/CoPB catalysts enhanced initially and then decreased. It is evident that MT/CoPB with a *B*/*P* ratio of 5 displayed optimal electrocatalytic activity for HER attributed to the low R_{ct} value of 3.1 Ω.

After identifying the optimal ratio (*B*/*P* = 5 and C : M = 2 : 1), the electrochemical activity of MT/CoPB was compared with control CoB, MT/CoB, and CoPB catalysts for HER. Bare GCE showed poor electrocatalytic activity, and standard Pt/C demonstrated an overpotential of −35 mV at a benchmark current density of 10 mA cm^{-2} for HER. The polarization curve shows an overpotential of −240, −173, −150, and −86 mV for CoB, MT/CoB, CoPB, and MT/CoPB, respectively. Among CoB and CoPB, the overpotential for CoPB is 90 mV less than the Co–B to reach a current density of 10 mA cm^{-2}. This shows that introducing P has resulted in increased activity due to a reduction in overpotential. Additionally, the inclusion of P in CoB not only increases the Co atoms on the surface but also enhances their activity through electron modulation, facilitating efficient water-splitting reactions.[38] In the case of CoB and MT/CoB, the

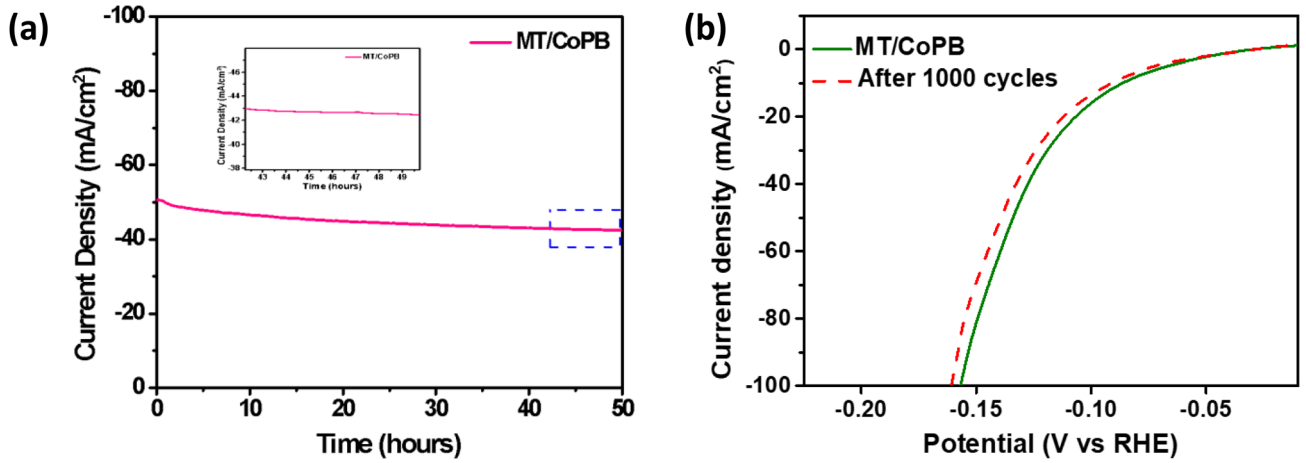

Fig. 5 (a) Chronoamperometric plot of MT/CoPB for HER (b) linear polarization curves for HER before and after 1000 cycles.

overpotential has reduced from −240 mV to −173 mV upon the addition of MT to highlight the promoting effect offered by MT to impact the electrocatalytic activity. These results align with the reduced overpotential observed in MT/CoPB compared to CoPB. Specifically, MT/CoPB showed an overpotential of −86 mV at 10 mA cm^{-2}, which is 64 mV lower compared to CoPB. These results show that the addition of carbon, as well as P into CoB, has significantly promoted the electrochemical performance of MT/CoPB, exhibiting a considerably low overpotential of −86 mV, which is approaching the overpotential of the noble Pt for HER.

The Tafel slope values for MT/CoPB, MT/CoB, CoPB, and CoB are 70, 101, 80 and 142 mV dec^{-1}, respectively. The lower Tafel slope of MT/CoPB implies fast reaction kinetics of the catalyst

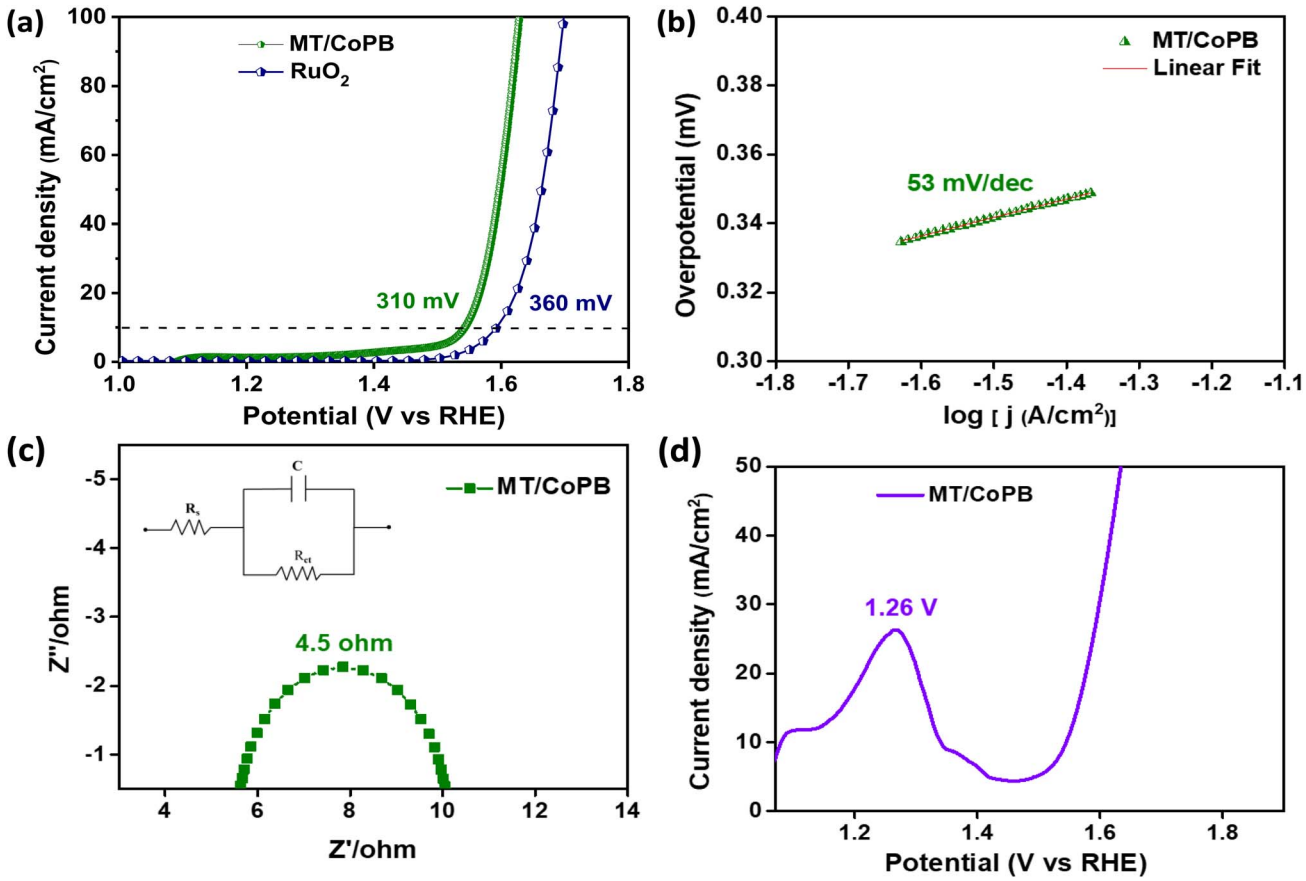

Fig. 6 (a) Linear polarization curves for OER (b) Tafel plot for OER (c) Nyquist plot for OER (d) linear polarization curve in the pre OER potential region.

towards HER through the Volmer–Heyrovsky mechanism.[52] EIS was performed for all catalysts to assess their relative charge transfer resistances. The obtained impedance data were fitted by an electrical equivalent circuit (inset of Fig. 4c) involving parallel RC components. Out of all the HER catalysts studied in this work, MT/CoPB has the least charge transfer resistance of 3.1 Ω, derived from Nyquist plots in comparison with CoB (7.8 Ω), CoPB (5.6 Ω), and MT/CoB (4 Ω). The lowest value of R_{ct} is reflected in the reduced overpotential for HER (Fig. 4a and c). In general, higher electrocatalytic performance is associated with a larger ECSA value, which is proportional to the electrochemical double-layer capacitance (C_{dl}). ECSA gives an assessment of the active sites present on the catalyst surface.[53] The C_{dl} value obtained from CV scans (Fig. S7a–d†) for CoB, MT/CoB, CoPB and MT/CoPB is depicted as 0.76, 3.6, 10, and 12.6 mF cm^{-2}, respectively. The higher C_{dl} values of MT/CoPB in comparison with MT/CoB, CoB, and CoPB (Fig. 4d) suggest a higher electrochemical surface area. This emphasizes the significant number of electrochemically active sites present, which leads to improved catalytic performance for MT/CoPB. Further the C_{dl} normalized LSV curves were plotted to probe the intrinsic activity of the catalysts. It was observed that in ECSA normalized curves (Fig. S8†), MT/CoPB remains the most effective catalyst showcasing the highest intrinsic activity per catalytic site. This reduced overpotential observed in MT/CoPB is due to the enhanced electrical conductivity, efficient electron transfer at the electrode/electrolyte interface, and the presence of a large amount of active site created by improved dispersion of CoPB particles on MT. Also, the mesoporous structure of the carbon allows better mass transport, improving the accessibility of reactants to the catalytic sites, which enhances overall catalytic activity and performance.[54] The formation of mesoporous structure was confirmed from the N_2 sorption isotherm (Fig. S9†). The graph exhibited type IV hysteresis with a noticeable hysteresis loop. The relative pressure (p/p_o) of 0.4 and 1.0, confirms the presence of mesopores and it suggests that synthesized MT is mesoporous in nature. MT acts as a support to anchor the CoPB which could be efficiently dispersed, which provides more active sites compared with individual CoPB catalysts. This is proved with increased ECSA of MT/CoPB in comparison with CoPB.

The stability of the electrocatalyst is one of the crucial factors for its practical application in real time. Thus, the electrochemical stability was evaluated by the chronoamperometric technique. The catalyst showed considerable stability for 50 h at a current density of 50 mA cm^{-2} (Fig. 5a). This confirms that the synthesized catalyst is stable and holds promise as an efficient candidate for HER. Moreover, the Nyquist plot of the MT/CoPB measured after stability testing (Fig. S10†) reveals minimal changes in the R_{ct} value before (3.1 Ω) and after (3.6 Ω) chronoamperometric test, further indicating the stability of the catalyst. The linear polarization curve after 1000 cycles is shown in Fig. 5b, indicating a negligible change in the catalyst's activity for HER even after 1000 cycles. Thus, the electrochemical tests confirmed that MT/CoPB serves as a stable and efficient electrocatalyst for HER in an alkaline medium. This result is attributed to the optimal ratio of carbon to CoPB, which not only provides high conductivity but also offers excellent dispersion of CoPB catalyst to improve ECSA.

The optimized catalyst MT/CoPB is also tested for OER to evaluate the bifunctional nature of the catalyst. LSV curves in the anode range acquired at a scan rate of 10 mV s^{-1} and corresponding Tafel slopes are shown in Fig. 6a and b, respectively. MT/CoPB requires an overpotential of 310 mV to reach the benchmark current density of 10 mA cm^{-2} and RuO_2 requires 360 mV for the same current density. This study revealed that MT/CoPB requires a lower overpotential in comparison to the standard catalyst for OER. The Tafel slope value of 53 mV dec^{-1} is recorded for MT/CoPB, demonstrating the faster reaction kinetics and low R_{ct} value of 4.5 Ω as obtained from the Nyquist plot (Fig. 6c). The formation of surface-active species (*OH and *OOH) is one of the factors influencing OER performance. It has been reported that metal borides and phosphides initially serve as pre-catalysts, facilitating the generation of active oxyhydroxide species.[55,56] LSV obtained at a slow scanning rate of 2 mV s^{-1} was used in order to study the formation of hydroxide/oxyhydroxide intermediates during the first OER cycle. In MT/CoPB, the peak for formation of CoOOH appears at 1.26 V with high intensity (Fig. 6d), thus suggesting that Co sites are converted to form CoOOH active species on the surface, leading to enhanced OER activity.[57] These tests demonstrated that MT/CoPB functions effectively as a catalyst for OER, showcasing its bifunctional nature.

To evaluate the structural stability of MT/CoPB after the HER and OER processes, FESEM images of the catalyst were analyzed post-reaction. The FESEM images (Fig. S11†) revealed that the morphology of the catalyst remained largely unchanged, indicating good structural stability. The observed agglomeration is likely attributable to the reaction conditions. The overall water-splitting performance of the MT/CoPB as a bifunctional electrocatalyst is evaluated using a two-electrode set-up, where MT/CoPB was assembled as a cathode and anode in 1 M KOH solution. The findings revealed that MT/CoPB reaches a current density of 10 mA cm^{-2} at a relatively low cell voltage of 1.59 V without *iR* correction, which is comparable to the standard

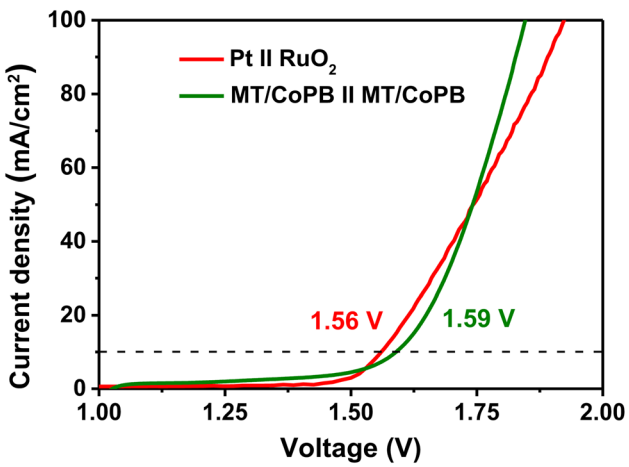

Fig. 7 Polarization curves in a two-electrode configuration for overall water splitting in alkaline medium.

Table 1 A comparison of electrochemical performance of cobalt and carbon-based electrocatalysts for HER and/or OER

Catalyst	HER overpotential at 10 mA cm^{-2}	OER overpotential at 10 mA cm^{-2}	Reference
Co@NC-A	−162	270	58
B,N,S–CoP@C@rGO	−112	264	59
Co/CoO@N@CC	−152	284	60
CoP@NC/NCN	−106	324	61
Co/BCTs-5	−74	330	62
Co@NGC-800	−234	304	63
Co0.15@ARC	−172	320	64
Co–B–P/g-C_3N_4	−174	—	65
MT/CoB	**−173**	**340**	**This work**
MT/CoPB	**−86**	**310**	**This work**

catalysts (Pt || RuO_2) with an overall cell voltage of 1.56 V (Fig. 7). The stability test for two electrode system was also tested and the catalyst MT/CoPB showed considerable stability as given in Fig S12.† This shows that MT/CoPB possesses good capabilities for overall water-splitting in an alkaline medium, making it a promising candidate for large-scale applications.

The Table 1 compares the electrochemical performance of MT/CoPB with other carbon-based, non-noble catalysts reported in the literature for HER and OER. The results suggest that the current electrocatalyst demonstrates activity that is better than or comparable to some of the benchmark electrocatalysts. MT/CoPB was synthesized using a simple, activation-free technique with a sustainable carbon source from biomass, making it both effective and economically viable.

Conclusions

In summary, this work provides an effective and simple, activation-free route for synthesizing biomass-derived carbon (MT) from mulberry bark and develops an optimized cobalt phospho-boride-based electrocatalyst (MT/CoPB) using a facile chemical reduction. The optimized MT/CoPB electrocatalyst ($B/P = 5$, $C:M = 2:1$) demonstrated superior bifunctional electrocatalytic activity for HER and OER in an alkaline medium. Detailed characterization revealed that the amorphous nature of MT/CoPB, coupled with its enhanced electrochemical surface area and favorable charge transfer properties, played a critical role in achieving high catalytic efficiency. For HER, MT/CoPB exhibited a low overpotential of 86 mV at a current density of 10 mA cm^{-2} and a Tafel slope of 70 mV dec^{-1}, indicating fast reaction kinetics. Similarly, for OER, MT/CoPB required an overpotential of only 310 mV to achieve the same current density, outperforming the benchmark RuO_2 catalyst. The catalyst demonstrated remarkable stability, maintaining its performance over prolonged chronoamperometric testing of 50 h and 1000 continuous cycles of operation. The catalyst also exhibited an overall cell potential of only 1.59 V when tested in a two-electrode assembly. The exceptional bifunctional activity of MT/CoPB can be attributed to its unique structural and compositional features, including well-dispersed CoPB nanoparticles on the carbon matrix, efficient electron transfer pathways, and the generation of active oxyhydroxide species during OER. The synthesis process, which utilized a sustainable carbon source from biomass, provides the economic and environmental viability of this approach. This work demonstrates that biomass-derived carbon nanosphere-based low-cost electrocatalysts offer a suitable alternative to traditional electrocatalysts, paving the way for future research in hydrogen production.

Author contributions

B. Sirichandana: conceptualization, methodology, investigation, visualization, writing – original draft, writing – reviewing and editing. R. Silviya: data curation, analysis, investigation, visualization. S. Venkataprasad Bhat: visualization, investigation. Nainesh Patel: writing – reviewing and editing, supervision. Gurumurthy Hegde: supervision, funding acquisition, writing – reviewing and editing.

Conflicts of interest

There are no conflicts to declare.

Data availability

The data supporting this article have been included as part of the ESI.†

Acknowledgements

One of the authors B. Sirichandana acknowledge the assistance provided by 'KSTePS, DST, Govt. of Karnataka. One of the authors Gurumurthy Hegde acknowledge Centre for Research Projects, CHRIST (Deemed to be University) for providing the seed money with the grant number SMSS-2214. S. Venkataprasad Bhat thanks SRM Institute of Science and Technology for the support and characterization facilities at SRM Central Instrumentation Facility as well as Nanotechnology Research Centre. N. Patel thanks the Department of Science and Technology, Ministry of Science and Technology, India, for providing funds under the AHFC project (DST/TMD-EWO/AHFC-2021/100), Indo-Italian Project (INT/Italy/P-42/2022(ER)(G)) and FIST program (SR/FST/PS-I/2022/208). N. Patel would like to acknowledge the Board of Nuclear Sciences, DAE, India, to fund the project (51/14/03/2023-BRNS/11376).

References

1 S. Chu and A. Majumdar, *Nature*, 2012, **488**, 294–303.
2 H. Ozcan, R. S. El-Emam, S. Celik and B. A. Horri, *Cleaner Chemical Engineering*, 2023, 100115.
3 T. Zhao, Y. Wang, S. Karuturi, K. Catchpole, Q. Zhang and C. Zhao, *Carbon Energy*, 2020, **2**, 582–613.
4 M. A. Rosen and S. Koohi-Fayegh, *Energy Ecol. Environ.*, 2016, **1**, 10–29.

5 Y. Yan, B. Y. Xia, B. Zhao and X. Wang, *J. Mater. Chem. A*, 2016, **4**, 17587–17603.
6 H. Kamaruddin, Z. Jianghong, L. Yu, W. Yuefan and H. Yizhong, *J. Mater. Chem. A*, 2024, **12**, 9933–9961.
7 S. Li, E. Li, X. An, X. Hao, Z. Jiang and G. Guan, *Nanoscale*, 2021, **13**, 12788–12817.
8 M. Khairy and K. G. Mahmoud, *J. Alloys Compd.*, 2023, **935**, 168056.
9 A. Guboova, R. Orinakova, M. Streckova, N. Podrojkova, M. Parackova, O. Milkovic, L. Medvecky, V. Girman and T. Bystron, *Electrochim. Acta*, 2024, **506**, 145008.
10 S. Aralekallu, K. Sannegowda Lokesh and V. Singh, *Fuel*, 2024, **357**, 129753.
11 Z. Chen, Y. Ha, Y. Liu, H. Wang, H. Yang, H. Xu, Y. Li and R. Wu, *ACS Appl. Mater. Interfaces*, 2018, **10**, 7134–7144.
12 Z. Xue, J. Kang, D. Guo, C. Zhu, C. Li, X. Zhang and Y. Chen, *Electrochim. Acta*, 2018, **273**, 229–238.
13 X. Xia, L. Wang, N. Sui, V. L. Colvin and W. W. Yu, *Nanoscale*, 2020, **12**, 12249–12262.
14 S. Gupta, N. Patel, A. Miotello and D. C. Kothari, *J. Power Sources*, 2015, **279**, 620–625.
15 N. K. Giddaerappa, U. Deshpande and L. K. Sannegowda, *Energy Fuels*, 2024, **38**, 8249–8261.
16 J. Hong, S. Mutalik, P. P. Pescarmona and L. Protesescu, *Chem. Mater.*, 2024, **36**, 2147–2164.
17 A. Ali, D. Akyüz, M. A. Asghar, A. Koca and B. Keskin, *Int. J. Hydrogen Energy*, 2018, **43**, 1123–1128.
18 S. S. Narwade, S. M. Mali, V. S. Sapner and B. R. Sathe, *ACS Appl. Nano Mater.*, 2020, **3**, 12288–12296.
19 Y. Huang, F. Tian, Y. Liu, M. Li, S. Xu, Y. Yu, J. Li, W. Yang and H. Li, *J. Colloid Interface Sci.*, 2022, **605**, 667–673.
20 Q. Hu, G. Li, Z. Han, Z. Wang, X. Huang, H. Yang, Q. Zhang, J. Liu and C. He, *J. Mater. Chem. A*, 2019, **7**, 14380–14390.
21 X. Chen, W. Li, C. Wang and X. Lu, *J. Colloid Interface Sci.*, 2023, **650**, 304–312.
22 Y. Yu, T. Wang, Y. Zhang, J. You, F. Hu and H. Zhang, *Chem. Rec.*, 2023, **23**, e202300109.
23 D. N. Sangeetha and M. Selvakumar, *Appl. Surf. Sci.*, 2018, **453**, 132–140.
24 M. Yang, F. Feng, K. Wang, S. Li, X. Huang, L. Gong, L. Ma and R. Li, *ChemSusChem*, 2020, **13**, 351–359.
25 J. Deng, M. Li and Y. Wang, *Green Chem.*, 2016, **18**, 4824–4854.
26 T. Sun, A. Fayad, A. Gomis-Berenguer and C. Ania, *Curr. Opin. Electrochem.*, 2024, **46**, 101511.
27 T. M. Nguyen, M. X. Tran, T. Van Nguyen, H. T. Dang, Q. V. Le, S. Y. Kim, T. P. Nguyen, D. H. Won and D. L. T. Nguyen, *Int. J. Hydrogen Energy*, 2024, **52**, 709–717.
28 B. Sukhbaatar, S. Yoon and B. Yoo, *J. Mater. Sci.*, 2022, **57**, 18075–18088.
29 Q. Wang, R. Yu, D. Shen, Q. Liu, K. Hong Luo, C. Wu and S. Gu, *Fuel*, 2023, **333**, 126368.
30 H. He, Y. Zhang, W. Zhang, Y. Li, Y. Wang, P. Wang and D. Hu, *ACS Appl. Mater. Interfaces*, 2021, **13**, 30678–30692.
31 A. Nieto-Márquez, R. Romero, A. Romero and J. L. Valverde, *J. Mater. Chem.*, 2011, **21**, 1664–1672.
32 Z. C. Kang and Z. L. Wang, *J. Phys. Chem.*, 1996, **100**, 5163–5165.
33 Y. Yao, J. Xu, Y. Huang and T. Zhang, *Particuology*, 2024, **87**, 325–338.
34 G. Soman, V. Molahalli, K. Sayeed, K. Pandey, B. B. Kulkarni and G. Hegde, *J. Energy Storage*, 2025, **111**, 115373.
35 A. Sharma, J. M. Shivanna, A. N. Alodhayb and G. Hegde, *Nanoscale Adv.*, 2024, **6**, 3199–3210.
36 P. Kanagavalli, G. R. Pandey, V. S. Bhat, M. Veerapandian and G. Hegde, *J. Nanostructure Chem.*, 2021, **11**, 343–352.
37 R. Silviya, Y. Vernekar, A. Bhide, S. Gupta, N. Patel and R. Fernandes, *ChemCatChem*, 2023, **15**, e202300635.
38 A. Chunduri, S. Gupta, O. Bapat, A. Bhide, R. Fernandes, M. K. Patel, V. Bambole, A. Miotello and N. Patel, *Appl. Catal., B*, 2019, **259**, 118051.
39 C. Chen, J. Zhu, S. Jia, S. Mi, Z. Tong, Z. Li, M. Li, Y. Zhang, Y. Hu and Z. Huang, *Energy*, 2018, **162**, 460–475.
40 S. Supriya, G. Sriram, Z. Ngaini, C. Kavitha, M. Kurkuri, I. P. De Padova and G. Hegde, *Waste Biomass Valorization*, 2020, **11**, 3821–3831.
41 S. Supriya, G. S. Ananthnag, V. S. Shetti, B. M. Nagaraja and G. Hegde, *Appl. Organomet. Chem.*, 2020, **34**, e5384.
42 K. Yu, J. Wang, X. Wang, J. Liang and C. Liang, *Mater. Chem. Phys.*, 2020, **243**, 122644.
43 S. Anantharaj and S. Noda, *Small*, 2020, **16**, e1905779.
44 D. Pathania, V. S. Bhat, J. Mannekote Shivanna, G. Sriram, M. Kurkuri and G. Hegde, *Spectrochim. Acta, Part A*, 2022, **276**, 121197.
45 J. Yang, H. Liu, W. N. Martens and R. L. Frost, *J. Phys. Chem. C*, 2010, **114**, 111–119.
46 X. Chen, X. Wang and D. Fang, Fullerenes Nanotubes, *Carbon Nanostruct.*, 2020, **28**, 1048–1058.
47 A. Bhaumik, A. Haque, M. F. N. Taufique, P. Karnati, R. Patel, M. Nath and K. Ghosh, *J. Mater. Sci. Eng.*, 2017, **6**, 364.
48 V. S. Bhat, S. G. Krishnan, T. J. Jayeoye, T. Rujiralai, U. Sirimahachai, R. Viswanatha, M. Khalid and G. Hegde, *J. Mater. Sci.*, 2021, **56**, 13271–13290.
49 Y. Jiang, Y. Fang, C. Chen, P. Ni, B. Kong, Z. Song, Y. Lu and L. Niu, *ChemElectroChem*, 2019, **6**, 3684–3689.
50 V. Jose, J. M. V. Nsanzimana, H. Hu, J. Choi, X. Wang and J.-M. Lee, *Adv. Energy Mater.*, 2021, **11**, 2100157.
51 M. A. Suliman, M. H. Suliman, A. Adam, C. Basheer, Z. H. Yamani and M. Qamar, *Mater. Lett.*, 2020, **268**, 127593.
52 R. Atchudan, S. Perumal, T. N. Jebakumar Immanuel Edison, A. K. Sundramoorthy, N. Karthik, S. Sangaraju, S. T. Choi and Y. R. Lee, *Catalysts*, 2023, **13**, 542.
53 A. Karmakar and S. Kundu, *Mater. Today Energy*, 2023, **33**, 101259.
54 X. Cao, Z. Li, H. Chen, C. Zhang, Y. Zhang, C. Gu, X. Xu and Q. Li, *Int. J. Hydrogen Energy*, 2021, **46**, 18887–18897.
55 S. Jin, *ACS Energy Lett.*, 2017, **2**, 1937–1938.
56 R. Silviya, A. Bhide, S. Gupta, R. Bhabal, K. H. Mali, B. R. Bhagat, M. Spreitzer, A. Dashora, N. Patel and R. Fernandes, *Small Methods*, 2024, **8**, e2301395.
57 A. Chunduri, S. Gupta, M. Patel, M. Forster, A. J. Cowan and N. Patel, *ChemSusChem*, 2020, **13**, 6534–6540.

58 W. Han, F. Zhang, Y. He, C. Yu, L. Lei and X. Zhang, *Electrochim. Acta*, 2024, **476**, 143735.
59 H. Xu, H. Jia, B. Fei, Y. Ha, H. Li, Y. Guo, M. Liu and R. Wu, *Appl. Catal., B*, 2020, **268**, 118404.
60 K. Dai, N. Zhang, L. Zhang, L. Yin, Y. Zhao and B. Zhang, *Chem. Eng. J.*, 2021, **414**, 128804.
61 Z. Wu, B. Liu, H. Jing, H. Gao, B. He, X. Xia, W. Lei and Q. Hao, *J. Colloid Interface Sci.*, 2023, **629**, 22–32.
62 E. Jiang, N. Song, S. Hong, M. Xiao, D. Zhu, Z. Yan, J. Sun, G. Chen, C. Li and H. Dong, *Electrochim. Acta*, 2022, **407**, 139895.
63 R. Kalusulingam, K. Ravi, S. Mathi, T. S. Mikhailova, K. Srinivasan, A. V. Biradar and T. N. Myasoedova, *Colloids Surf., A*, 2024, **692**, 133959.
64 Y. Zhou, Y. Luo, Q. Li, J. Liang, F. Liu, Y. Cai, L. Lin, Q. Wu and K. Li, *Energy Fuels*, 2024, **38**, 15560–15570.
65 Q. He, L. Wang, F. Xiao, R. Su, Y. Jiang, L. Chen, Z. Wang, B. Jia, P. He, C. Chen, Y. Zeng, Y. Zhou and B. Tang, *Int. J. Hydrogen Energy*, 2024, **58**, 149–157.